LETTER

doi:10.1038/nature13006

Amazon forests maintain consistent canopy structure and greenness during the dry season

Douglas C. Morton[1], Jyoteshwar Nagol[2,3], Claudia C. Carabajal[1,4], Jacqueline Rosette[1,2,5], Michael Palace[6], Bruce D. Cook[1], Eric F. Vermote[1], David J. Harding[1] & Peter R. J. North[5]

The seasonality of sunlight and rainfall regulates net primary production in tropical forests[1]. Previous studies have suggested that light is more limiting than water for tropical forest productivity[2], consistent with greening of Amazon forests during the dry season in satellite data[3–7]. We evaluated four potential mechanisms for the seasonal green-up phenomenon, including increases in leaf area[5–7] or leaf reflectance[3,4,6], using a sophisticated radiative transfer model[8] and independent satellite observations from lidar and optical sensors. Here we show that the apparent green up of Amazon forests in optical remote sensing data resulted from seasonal changes in near-infrared reflectance, an artefact of variations in sun-sensor geometry. Correcting this bidirectional reflectance effect eliminated seasonal changes in surface reflectance, consistent with independent lidar observations and model simulations with unchanging canopy properties. The stability of Amazon forest structure and reflectance over seasonal timescales challenges the paradigm of light-limited net primary production in Amazon forests and enhanced forest growth during drought conditions. Correcting optical remote sensing data for artefacts of sun-sensor geometry is essential to isolate the response of global vegetation to seasonal and interannual climate variability.

The role of Amazon forests in the global carbon budget remains uncertain[9–12]. Efforts to better constrain net carbon emissions from Amazonia have focused on the magnitude of deforestation carbon fluxes[13] and the seasonal and interannual variability of Amazon forest productivity[1,14–16]. Variability in Amazon forest productivity is potentially larger than deforestation emissions on an annual basis, yet remains poorly constrained by field[14,16] or atmospheric observations[11,12]. At the centre of this debate is whether tropical forest productivity is more limited by sunlight or rainfall[3,4,9,14,16,17]. Resolving this issue is critical to reducing uncertainties in the contemporary carbon balance of tropical forests[10–12,15,16] and the probable response of Amazon forests to climate change[9,18,19].

Satellite instruments offer a global perspective on seasonal and interannual changes in vegetation productivity. Indices of fractional vegetation cover derived from satellite data suggest a 'green up' over Amazon forests during the dry season[3,17], consistent with the light limitation hypothesis[2]. Previous studies have attributed this seasonal greening of Amazon forests to synchronous canopy leaf turnover[3,4,6], as young leaves reflect more near-infrared (NIR) light than the older leaves they replace[20], or seasonal increases in green leaf area[5–7]. These leaf-level responses would increase the photosynthetic capacity of Amazon forests, resulting in higher net primary production (NPP) as photosynthetically active radiation (PAR) increases during dry season months[1,3,4]. Light-limited forests could therefore respond to drought events or other cloud-free periods with an increase in NPP[17], given sufficient access to deep soil moisture[21].

NASA's Moderate Resolution Imaging Spectroradiometer (MODIS) is the primary data source for studies of the green-up phenomenon, including the enhanced vegetation index (EVI)[3,4,7] and leaf area index (LAI) products[5,7]. The MODIS EVI and LAI products are very sensitive to changes in NIR reflectance[7,22]. Several mechanisms could generate an increase in the NIR reflectance of Amazon forests (Table 1); increases in MODIS EVI or LAI alone are therefore insufficient to isolate the biophysical basis for the Amazon green up[6,7].

We combined three lines of evidence to test the hypotheses that changes in leaf area or leaf reflectance drive the appearance of a seasonal green up of forests in southern Amazonia. First, we synthesized a three-dimensional Amazon forest (Extended Data Fig. 1) and used the FLIGHT radiative transfer model[8] to simulate changes in lidar and optical remote sensing metrics from seasonal variability in leaf and litter reflectances, leaf area, and sun-sensor geometry during the June to October dry season (Table 1). Second, we analysed lidar waveform centroid relative height (WCRH)[23] and 1064 nm retroreflectance measurements from the Geosciences Laser Altimeter System (GLAS) lidar instrument onboard NASA's Ice, Cloud, and land Elevation satellite (ICESat)[24]. GLAS footprint pairs were selected from adjacent orbits in June and October across the southern Amazon. Finally, we reprocessed daily surface reflectance data at 1 km spatial resolution from the Terra and Aqua MODIS sensors to eliminate artefacts from changes in sun-sensor geometry. The combination of theoretical modelling and independent lidar and optical satellite observations in this study generated multiple lines of evidence to better characterize the apparent green-up phenomenon. We found no evidence for consistent seasonal changes in canopy structure or reflectance properties of southern Amazon forests from lidar and optical remote sensing observations. Our approach to constrain seasonal variability in NIR reflectance has wide-ranging implications

Table 1 | Lidar and optical remote sensing metrics are sensitive to possible leaf-level mechanisms for a seasonal green up of Amazon forests

Model simulations	WCRH	EVI	NDVI
June*	0.52	0.40	0.87
October†			
Sun-sensor geometry		0.43	0.81
ρLitter (+20–25%)‡	0.48	0.48	0.83
ρLeaf (+10%)	0.52	0.54	0.85
LAI (+2)	0.58	0.43	0.83
LAI + ρLitter	0.56	0.46	0.84
LAI + ρLeaf	0.58	0.55	0.87
LAI + ρLeaf + ρLitter	0.56	0.59	0.88

Model simulations evaluated the impact of seasonal changes in sun-sensor geometry and increases in litter reflectance (ρLitter), leaf reflectance (ρLeaf), and leaf area index (LAI) on GLAS lidar WCRH and MODIS vegetation indices (EVI, NDVI).

* Amazon forest conditions in June for FLIGHT radiative transfer model simulations of GLAS lidar (LAI = 4.5, 1064 nm ρLeaf = 0.39, and 1064 nm ρLitter = 0.34) and MODIS surface reflectance, uncorrected for sun-sensor geometry (LAI = 4.5, 860 nm ρLeaf = 0.39, 860 nm ρLitter = 0.30; and mean Terra MODIS solar zenith angle (θ_s) = 40°, view zenith angle (θ_v) = 15°, and relative azimuth (ϕ) = 60°).

† October viewing conditions for MODIS simulations were $\theta_s = 20°$, $\theta_v = 15°$, $\phi = 0°$.

‡ ρLitter was increased by 20% for lidar (0.54) and 25% (0.55) for optical simulations with FLIGHT (see Extended Data Fig. 1).

[1]NASA Goddard Space Flight Center, Greenbelt, Maryland 20771, USA. [2]University of Maryland, College Park, Department of Geographical Sciences, College Park, Maryland 20742, USA. [3]Global Land Cover Facility, College Park, Maryland 20740, USA. [4]Sigma Space Corporation, Lantham, Maryland 20706, USA. [5]Swansea University, Department of Geography, Singleton Park, Swansea SA2 8PP, UK. [6]Earth System Research Center, University of New Hampshire, Durham, New Hampshire 03824, USA.

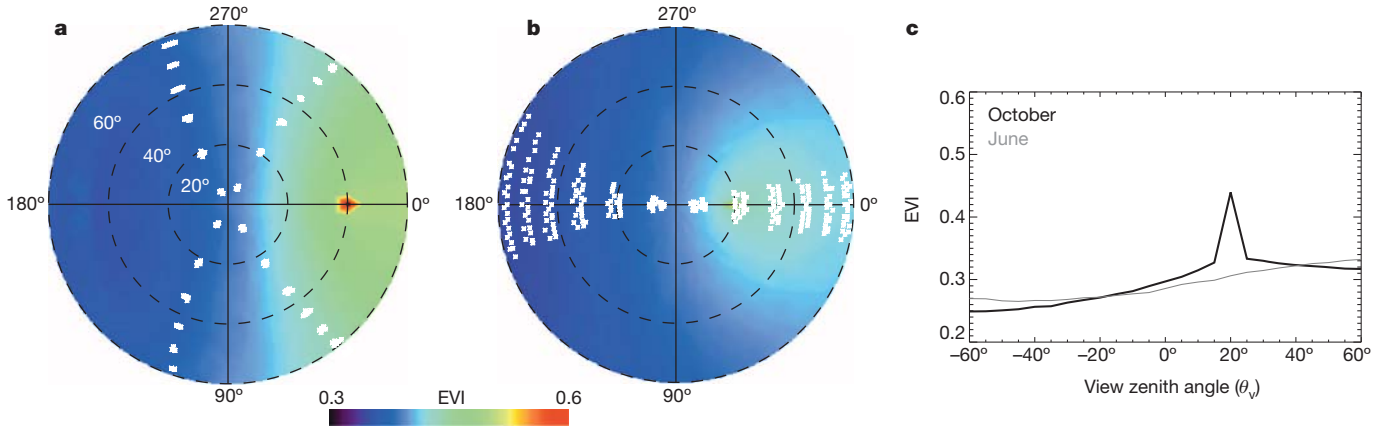

Figure 1 | Seasonal changes in sun-sensor geometry generate the appearance of a green up in MODIS observations of Amazon forest between June and October. **a**–**c**, Modelled directional anisotropy of the MODIS enhanced vegetation index (EVI) is stronger in June (**a**) than October (**b**), but the realized bidirectional reflectance effect is greater in October (**b**, **c**) when the MODIS instruments sample in the principal plane ($\phi = 0°$, $\phi = 180°$). White dots in **a** and **b** indicate the relative azimuth angle of Terra and Aqua MODIS observations. The peak in modelled October EVI near $\theta_v = 20°$ indicates the hot-spot effect from the alignment of solar illumination and sensor observation angles.

for *in situ*, airborne and satellite-based studies of vegetation phenology and canopy structure that rely on NIR spectral information.

Three potential biophysical mechanisms for a green up of Amazon forests generated unique responses in modelled lidar and optical remote sensing metrics (Table 1 and Extended Data Table 1). Increasing litter reflectance, consistent with greater litter depth or lower litter moisture during the dry season, decreased the WCRH and increased EVI. Increasing leaf reflectance had negligible effects on WCRH based on compensating increases in both single and multiple scattering of NIR photons, but led to a 32–35% increase in EVI relative to simulations with unchanging canopy properties. Adding LAI increased both WCRH and EVI, as did combinations of increasing LAI, leaf reflectance and litter reflectance. A fourth mechanism, changes in sun-sensor geometry, only influenced simulations of MODIS reflectance data. During the Amazon dry season, the relative azimuth angle (ϕ) of MODIS observations decreases until the sensor approaches the principal plane ($\phi = 0°$, $\phi = 180°$) following the September equinox (Fig. 1 and Extended Data Fig. 3). Changes in sun-sensor geometry alone increased EVI across the range of view zenith angles selected for most land applications (Fig. 1). Modelled changes were greatest near the hot spot, although the magnitude of the hot-spot effect is difficult to reproduce in a theoretical model[25]. Seasonal changes in sun-sensor geometry decreased the modelled normalized difference vegetation index (NDVI) due to an increase in red reflectance in the hot spot (Table 1 and Extended Data Fig. 4). The magnitude of changes in modelled and observed MODIS NDVI was smaller than for EVI (see Supplementary Information). Results of the FLIGHT model simulations indicated that combined information from lidar and optical satellite sensors could isolate leaf or litter mechanisms for seasonal greening from artefacts of changing sun-sensor geometry in MODIS observations.

The distributions of relative heights and apparent reflectance estimates from GLAS lidar observations did not increase between June and October across the southern Amazon (Fig. 2). Consistent WCRH values at the beginning and end of the dry season could occur despite increasing leaf reflectance (Table 1). However, the distribution of the most reflective lidar returns was also similar between June and October, indicating that the overall reflectivity of the forests at 1064 nm did not increase. Combined, height and reflectance estimates from the GLAS lidar instrument do not provide consistent regional evidence for a leaf-level mechanism for seasonal greening of Amazon forests.

The spatial patterns of lidar metrics also differed from previous maps of the Amazon green-up phenomenon. Distributions of GLAS lidar WCRH in June and October were similar across the southern Amazon (Extended Data Fig. 5). As a relative metric, WCRH is more robust to residual atmospheric contamination from biomass burning that may influence lidar apparent reflectance estimates over Amazon forests. The spatial pattern of WCRH estimates during the dry season highlights greater penetration of lidar energy in forests with lower mean annual precipitation (Extended Data Fig. 6). We speculate that lower WCRH estimates in these drier forest regions may arise from greater vertical heterogeneity from emergent trees or higher gap fraction because of moisture competition. A higher degree of within-canopy shadowing in forests with low WCRH could exacerbate the directional anisotropy in surface reflectance from optical sensors such as MODIS.

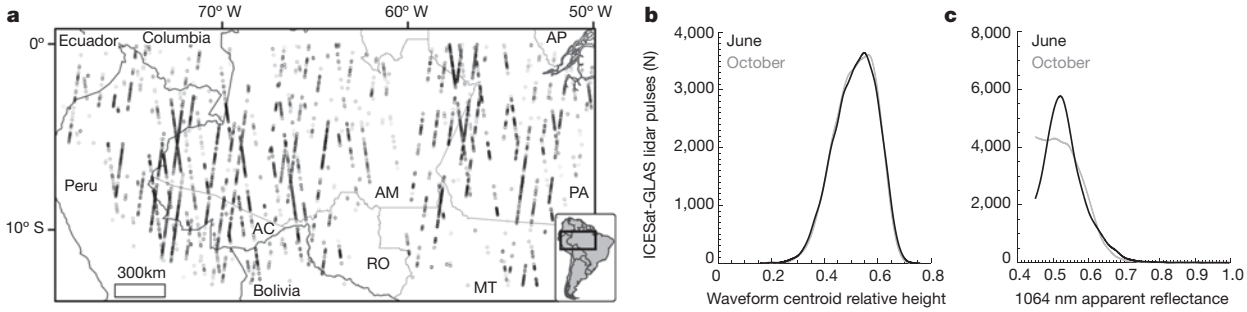

Figure 2 | Independent GLAS lidar observations indicate consistent canopy properties between June and October across southern Amazonia. **a**, Map of GLAS lidar footprint pairs from adjacent orbits during June (L3c and L3f) and October (L3a and L3i) laser operation periods ($n = 74{,}638$). **b**, **c**, Distributions of lidar waveform centroid relative heights (WCRH) (**b**) and maximum apparent reflectance (**c**) (1064-nm retroreflectance) did not increase between early and late dry season laser operation periods. States within the Brazilian Amazon are abbreviated in **a**. Acre, AC; Amazonas, AM; Amapá, AP; Mato Grosso, MT; Pará, PA; Rondônia, RO.

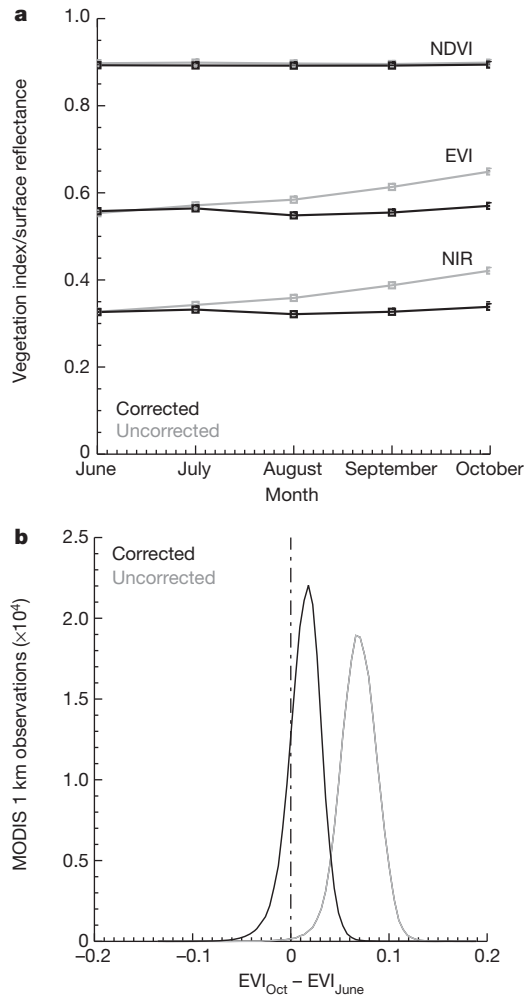

Figure 3 | Seasonal increases in MODIS near-infrared reflectance (NIR) and enhanced vegetation index (EVI) data were eliminated after normalizing sun-sensor geometry during the June to October dry season. **a**, Seasonal profile of the normalized difference vegetation index (NDVI), EVI and NIR for uncorrected (grey) and corrected (black) MODIS data in southern Amazonia. Values indicate the upper quartile median monthly NDVI, EVI and NIR of all Terra and Aqua MODIS observations in 2003–08 ($n = 197{,}651$). **b**, Per-pixel changes in uncorrected (grey) and corrected (black) MODIS EVI between October and June for forested areas in southern Amazonia.

Removing artefacts of changing sun-sensor geometry in MODIS red and NIR reflectance data eliminated the appearance of a green up in MODIS EVI during dry season months (Fig. 3 and Extended Data Fig. 7). Previous green-up studies with MODIS EVI or LAI data did not explicitly account for changing viewing and illumination conditions[3,7,17] or did not normalize to a constant sun-sensor geometry for all observations[4]. Corrected EVI data also eliminated the appearance of interannual variability during 2003–08 (Extended Data Fig. 8). Artefacts from changes in sun-sensor geometry during the dry season may therefore explain previous reports of higher EVI values over Amazon forests during drought conditions[17]. Indeed, lower cloud cover during drought years increases the probability of observing forests in the southern Amazon when MODIS observations are closer to the principal plane (Extended Data Fig. 9).

Seasonal increases in NIR reflectance drive the apparent green up of Amazon forests, based on a reduction in self-shading near the September equinox that is amplified in MODIS EVI data by changes in sun-sensor geometry. Seasonal changes in NIR reflectance and EVI do not correspond directly to changes in leaf reflectance, leaf area or vegetation productivity. However, the sensitivity of uncorrected MODIS EVI to seasonal illumination may serve as a useful proxy for variability in the fraction of absorbed PAR (FAPAR). This relationship between EVI and FAPAR may explain the positive correlation between MODIS EVI and net ecosystem exchange (NEE) in Amazon forests[3] and other biomes[26]. The potential response of Amazon forests to increasing PAR in the dry season, as measured at the top of canopy[1], is therefore moderated by seasonal variability in FAPAR from the reduction in self-shading between the June solstice and September equinox.

Satellite-based evidence for consistent reflectance of Amazon forest canopies over seasonal and annual time scales reframes the debate over climate controls on Amazon forest productivity. Leaf turnover may still be important for increased productivity of individual trees during dry season months[4,6,19,20], but GLAS and MODIS observations do not support the hypotheses that changes in canopy reflectance properties from leaf phenology are consistent at larger spatial scales ($\geq$1 km) across the southern Amazon. Direct observations of this fine-scale variability in Amazon forest NPP may yet be possible from satellite-based estimates of vegetation fluorescence[27] or light-use efficiency[28], provided that the fraction of sunlit and shaded leaf area can be retrieved or modelled simultaneously. Our results support the initial interpretations of eddy covariance studies[1], rainfall exclusion experiments[29] and plot measurements[14] in Amazon forests that seasonal moisture availability governs the balance between photosynthesis and respiration in Amazon forests.

METHODS SUMMARY

A 1 km^2 Amazon forest was synthesized using field measurements of forest structure and reflectance properties (see Extended Data Fig. 1). Tree locations and attributes were used to generate a three-dimensional forest scene in the FLIGHT radiative transfer model[8]. FLIGHT model simulations quantified the impact of individual and combined seasonal changes in leaf reflectance, litter reflectance, LAI, and MODIS relative azimuth angle on optical and lidar remote sensing metrics (see Extended Data Figs 1 and 2 and Extended Data Table 1). Simulated seasonal changes in remote sensing metrics were compared with GLAS and MODIS observations.

ICESat-GLAS lidar data over southern Amazon forests were selected from Laser 3 operation periods in the early (L3c, May to June 2005; L3f, May to June 2006) and late dry seasons (L3a, October 2004; L3i, October 2007). GLAS waveform characteristics were derived from the GLA09 and GLA14 standard products (data access: http://nsidc.org). High-quality data from adjacent orbits in June and October were used to assess seasonal changes in lidar apparent reflectance and WCRH[23] ($n = 74{,}638$).

Terra and Aqua MODIS daily 1 km surface reflectance data from 2003–08 were acquired for two $10^\circ \times 10^\circ$ spatial tiles (H11V09 and H12V09, Collection 5 MOD09GA and MYD09GA, data access: https://lpdaac.usgs.gov/). Each month, high-quality Terra and Aqua MODIS data were combined to estimate the bidirectional reflectance distribution function (BRDF) and perform a per-pixel correction for variations in sun-sensor geometry[25]. A threshold of $\geq$ 20 observations per pixel, per month was set to ensure a robust statistical inversion ($n = 197{,}651$). BRDF parameters were used to normalize red and NIR reflectance values to constant solar ($\theta_s = 30^\circ$) and view geometries ($\theta_v = 0^\circ$). NDVI and a two-band version of EVI[30] were calculated using the normalized red and NIR reflectance data. Uncertainties in normalized MODIS data were assessed using a Monte Carlo sensitivity analysis.

Online Content Any additional Methods, Extended Data display items and Source Data are available in the online version of the paper; references unique to these sections appear only in the online paper.

Received 19 December 2012; accepted 8 January 2014.
Published online 5 February 2014.

1. Saleska, S. R. *et al.* Carbon in Amazon forests: unexpected seasonal fluxes and disturbance-induced losses. *Science* **302,** 1554–1557 (2003).
2. Nemani, R. R. *et al.* Climate-driven increases in global terrestrial net primary production from 1982 to 1999. *Science* **300,** 1560–1563 (2003).
3. Huete, A. R. *et al.* Amazon rainforests green-up with sunlight in dry season. *Geophys. Res. Lett.* **33,** L06405 (2006).
4. Brando, P. M. *et al.* Seasonal and interannual variability of climate and vegetation indices across the Amazon. *Proc. Natl Acad. Sci. USA* **107,** 14685–14690 (2010).
5. Myneni, R. B. *et al.* Large seasonal swings in leaf area of Amazon rainforests. *Proc. Natl Acad. Sci. USA* **104,** 4820–4823 (2007).

6. Doughty, C. E. & Goulden, M. L. Seasonal patterns of tropical forest leaf area index and CO_2 exchange. *J. Geophys. Res.* **113,** G00B06 (2008).
7. Samanta, A. *et al.* Seasonal changes in leaf area of Amazon forests from leaf flushing and abscission. *J. Geophys. Res.* **117,** G01015 (2012).
8. North, P. R. J., Rosette, J. A. B., Suarez, J. C. & Los, S. O. A Monte Carlo radiative transfer model of satellite waveform LiDAR. *Int. J. Remote Sens.* **31,** 1343–1358 (2010).
9. Davidson, E. A. *et al.* The Amazon basin in transition. *Nature* **481,** 321–328 (2012).
10. Pan, Y. *et al.* A large and persistent carbon sink in the world's forests. *Science* **333,** 988–993 (2011).
11. Chevallier, F. *et al.* Global CO_2 fluxes inferred from surface air-sample measurements and from TCCON retrievals of the CO_2 total column. *Geophys. Res. Lett.* **38,** L24810 (2011).
12. Gatti, L. V. *et al.* Vertical profiles of CO_2 above eastern Amazonia suggest a net carbon flux to the atmosphere and balanced biosphere between 2000 and 2009. *Tellus B Chem. Phys. Meterol.* **62,** 581–594 (2010).
13. van der Werf, G. R. *et al.* CO_2 emissions from deforestation. *Nature Geosci.* **2,** 737–738 (2009).
14. Phillips, O. L. *et al.* Drought sensitivity of the Amazon rainforest. *Science* **323,** 1344–1347 (2009).
15. Le Quére, C. *et al.* Trends in the sources and sinks of carbon dioxide. *Nature Geosci.* **2,** 831–836 (2009).
16. Lewis, S. L., Brando, P. M., Phillips, O. L., van der Heijden, G. M. F. & Nepstad, D. The 2010 Amazon drought. *Science* **331,** 554 (2011).
17. Saleska, S. R., Didan, K., Huete, A. R. & da Rocha, H. R. Amazon forests green-up during 2005 drought. *Science* **318,** 612–612 (2007).
18. Zelazowski, P., Malhi, Y., Huntingford, C., Sitch, S. & Fisher, J. B. Changes in the potential distribution of humid tropical forests on a warmer planet. *Phil. Trans. Royal Soc. A* **369,** 137–160 (2011).
19. Kim, Y. *et al.* Seasonal carbon dynamics and water fluxes in an Amazon rainforest. *Glob. Change Biol.* **18,** 1322–1334 (2012).
20. Toomey, M., Roberts, D. A. & Nelson, B. The influence of epiphylls on remote sensing of humid forests. *Remote Sens. Environ.* **113,** 1787–1798 (2009).
21. Nepstad, D. C. *et al.* The role of deep roots in the hydrological and carbon cycles of Amazonian forests and pastures. *Nature* **372,** 666–669 (1994).
22. Galvão, L. S. *et al.* On intra-annual EVI variability in the dry season of tropical forest: a case study with MODIS and hyperspectral data. *Remote Sens. Environ.* **115,** 2350–2359 (2011).
23. Carabajal, C. C. & Harding, D. J. SRTM C-Band and ICESat laser altimetry elevation comparisons as a function of tree cover and relief. *Photogramm. Eng. Remote Sensing* **72,** 287–298 (2006).
24. Schutz, B. E., Zwally, H. J., Shuman, C. A., Hancock, D. & DiMarzio, J. P. Overview of the ICESat mission. *Geophys. Res. Lett.* **32,** L21S01 (2005).
25. Bréon, F.-M., Maignan, F., Leroy, M. & Grant, I. Analysis of hot spot directional signatures measured from space. *J. Geophys. Res.* **107,** http://dx.doi.org/10.1029/2001JD001094 (2002).
26. Rahman, A. F., Sims, D. A., Cordova, V. D. & El-Masri, B. Z. Potential of MODIS EVI and surface temperature for directly estimating per-pixel ecosystem C fluxes. *Geophys. Res. Lett.* **32,** L19404 (2005).
27. Joiner, J., Yoshida, Y., Vasilkov, A. P., Corp, L. A. & Middleton, E. M. First observations of global and seasonal terrestrial chlorophyll fluorescence from space. *Biogeosciences* **8,** 637–651 (2011).
28. Hilker, T. *et al.* Inferring terrestrial photosynthetic light use efficiency of temperate ecosystems from space. *J. Geophys. Res.* **116,** G03014 (2011).
29. Nepstad, D. C., Tohver, I. M., Ray, D., Moutinho, P. & Cardinot, G. Mortality of large trees and lianas following experimental drought in an Amazon forest. *Ecology* **88,** 2259–2269 (2007).
30. Jiang, Z., Huete, A. R., Didan, K. & Miura, T. Development of a two-band enhanced vegetation index without a blue band. *Remote Sens. Environ.* **112,** 3833–3845 (2008).

Supplementary Information is available in the online version of the paper.

Acknowledgements Funding for this research was provided by NASA, the NASA Postdoctoral Program and the NERC National Centre for Earth Observation. We thank G. P. Asner for providing Amazon leaf reflectance data.

Author Contributions D.C.M. and J.N. designed the experiment. D.C.M., J.N. and E.F.V. analysed MODIS data. D.C.M., C.C.C., B.D.C. and D.J.H. analysed ICESat data. M.P. developed the synthetic forest model. D.C.M., J.N., J.R., B.D.C. and P.R.J.N. contributed to radiative transfer model simulations. D.C.M. wrote the manuscript, and all authors contributed material to the final version.

Author Information Data from NASA's ICESat, Terra, and Aqua satellites are archived at http://www.nsidc.org and http://lpdaac.usgs.gov. Reprints and permissions information is available at www.nature.com/reprints. The authors declare no competing financial interests. Readers are welcome to comment on the online version of the paper. Correspondence and requests for materials should be addressed to D.C.M. (douglas.morton@nasa.gov).

METHODS

Synthetic Amazon forest. We synthesized an Amazon forest scene for radiative transfer model simulations using a three-dimensional canopy model and field measurements of forest structure (Extended Data Fig. 1). The modelled forest was generated using allometric equations for the relationships between diameter at breast height (*dbh*), canopy height (h), crown width (C_w), and crown depth (C_d). For trees >20-cm diameter at breast height, we used published allometric equations for the eastern Amazon[31–33]. Log-linear relationships derived from field measurements of large trees provided unrealistic values for smaller trees, especially stems <10-cm diameter at breast height. Therefore, we adjusted the allometric relationships to better represent smaller diameter stems in the synthetic forest scene.

In the forest understory, crown dimensions are more strongly correlated with h than *dbh*[34,35]. We adjusted the original h-*dbh* relationships for small trees, using the large-tree allometry estimates for trees 10–25-cm diameter at breast height. These original estimates were fit with a power-law function to estimate the h (m) of trees with diameter at breast height < 20 cm (Extended Data Fig. 1):

$$h = 1.37 dbh^{0.88}$$

Adjusted h estimates for small diameter trees were then used to develop revised estimates of C_w and C_d. The resulting h-C_w relationship was close to the reported values for a range of understory species in Panama[34]:

$$C_w = 0.47 h^{0.934}$$

A revised estimate of C_d for small trees was derived in similar fashion, based on a power-law fit of the h-C_d relationship for trees 25–50-m in height. Larger trees were selected for estimating C_d in small trees because the h-C_d relationship for trees 10–25-m was asymptotic:

$$C_d = 0.11 h^{1.5}$$

This approach resulted in a flattening of tree crowns in the understory, with C_d estimates of 10, 30, and 60 cm for trees 1, 2 and 3 m in height, respectively.

We synthesized an Amazon forest scene with 8% gap fraction and 200 trees per hectare (ha), similar to satellite and field-based studies in eastern Amazonia, respectively[32,36]. Trees were drawn at random from a Weibull distribution of diameter at breast height sizes to populate a 1 × 1 km forest scene (Extended Data Fig. 1). Weibull distribution parameters ($\beta = 1$, $\alpha = 27.5$-cm diameter at breast height) were based on an extensive survey (392 ha) of diameter at breast height values in the Tapajos National Forest near Santarém, Pará[31,36]. Trees were located in x,y space using a simple spacing algorithm. If more than half of the crown radius of the new individual overlapped with half of the crown radius of an existing tree, the tree was excluded and a new sample was drawn until the stem density reached 20,000 individuals >1-cm diameter at breast height per km^2. Conceptually, this approach incorporates the concepts of shading (large trees exclude small trees) and gap dynamics (small trees indicate the absence of large trees). The x,y location and properties of each stem (*dbh*, h, C_w, C_d) were used to create a three-dimensional forest scene in the FLIGHT model[8]. We estimated mean total aboveground biomass of 312 megagrams carbon per ha for the synthetic forest scene based on an independent height-diameter allometry[37], similar to forest inventory data[36] and satellite-based estimates[38,39] of above-ground biomass in the eastern Amazon.

FLIGHT model simulations. We simulated the impact of seasonal changes in Amazon forest structure and reflectance properties on optical and lidar remote sensing metrics using FLIGHT, a three-dimensional model of light transport based on a Monte Carlo simulation of radiative transfer[8,40]. FLIGHT uses photon trajectories within a canopy to evaluate solar bidirectional reflectance and lidar backscatter retroreflectance (reflectance at 0° phase angle). The model simulates the chain of scattering events along each photon trajectory, including multiple scattering between canopy elements and the ground surface. Atmospheric transmittance is simulated using fixed conditions for atmospheric trace gases and aerosols. Amazon tree crowns were modelled as elliptical shells, and field measurements[41] of reflectance and transmittance (Extended Data Fig. 1) were assigned to scattering elements based on the proportion of leaves (85%) and branches (15%) within each crown. To simulate seasonal increases in LAI, only the foliar area was increased in each canopy, thereby decreasing the relative fraction of bark and branches.

Optical and lidar radiative transfer simulations quantified the impact of seasonal changes in leaf reflectance (ρLeaf, ± 10%), litter reflectance (ρLitter, ± 10–25%), and LAI (+1, +2) on remote sensing metrics. Multiple changes in seasonal forest structure and reflectance were simulated using combinations of ρLeaf, ρLitter, and LAI changes under October illumination conditions (Table 1 and Extended Data Table 1). Optical simulations also considered MODIS viewing geometry and seasonal variability in solar illumination, based on the location of the simulated Amazon forest (2.65° S, 54.95° W). FLIGHT simulations with varying relative azimuth angle (ϕ, 0°–180°), view zenith angle (θ_v, 0°–60°), and solar zenith angle (θ_s, 20°–40°) provided a more complete picture of the directional anisotropy of surface reflectance from seasonal illumination conditions. These three-dimensional plots of the bidirectional reflectance effect were used to illustrate the impact of seasonal changes in sun-sensor geometry on optical remote sensing data (Fig. 1 and Extended Data Fig. 4).

Lidar radiative transfer simulations with FLIGHT incorporated GLAS instrument characteristics, including nadir incidence angle, 5-ns pulse duration, 57 mJ pulse energy (Laser 3a), 600 km sensor altitude and 450 μrad detector field of view. In addition, a constant 5° slope was added to the Amazon forest scene to simulate the effect of microtopography on laser energy returned from the ground. The distribution of modelled WCRH for the synthetic Amazon forest was similar to GLAS data (Fig. 2 and Extended Data Fig. 2a). However, lidar simulations were conducted using a single footprint to isolate the influence of individual scene modifications on lidar radiative transfer (Extended Data Fig. 2b).

Random background noise, similar to noise levels in GLAS lidar waveforms, was added to FLIGHT lidar waveforms to simulate a realistic signal returned to the detector. Noise levels were consistent with the potential contribution from solar photons to return waveform energy, based on FLIGHT simulations of the solar flux at 1064 nm for solar noon at the equator under June and October illumination conditions (0.8–2.5%). Solar noise constitutes a constant offset term in the vertical lidar waveform and does not impact the relative metrics derived from modelled or observed lidar waveforms. The extent of the forest canopy was determined by setting an amplitude threshold above the background noise, based on the signal-to-noise characteristics of the waveform. A Gaussian smoothing algorithm was used as a low-pass filter before computing lidar metrics, following established waveform-processing methods[42]. The width of the smoothing Gaussian was chosen as the half-width at full maximum of the outgoing laser pulse to avoid over-smoothing the waveform data. The ground peak maximum was detected by determining the zero-crossing point of the first derivative of the smoothed waveform.

ICESat-GLAS lidar analysis. GLAS lidar data provided an independent estimate of seasonal changes in forest structure and canopy reflectance. The GLAS instrument is a large footprint, full-waveform lidar[24,43]. Each lidar waveform contains information on the height and vertical distribution of scattering elements within the lidar footprint, and the integrated energy from the return waveform can be normalized by the outgoing laser energy to estimate apparent reflectance at 1064 nm. Apparent reflectance corresponds to the footprint retroreflectance multiplied by the square of atmospheric transmission to account for the two-way travel path. The waveform centroid relative height (WCRH)[23] was used in this study to assess changes in the relative height of median energy within the waveform:

$$WCRH = \frac{(CE - S_eE)}{(S_sE - S_eE)}$$

where CE corresponds to the waveform centroid elevation, S_sE is the signal start elevation and S_eE is the signal end elevation as determined by thresholds defined for the alternate (land) waveform processing schemes. GLAS footprints over Amazon forest cover types were selected based on time series of dry season MODIS NDVI data[44] to select forests >1 km from non-forest cover types and burned forest areas in 2010 (ref. 45). In addition, topographic data from the Shuttle Radar Topography Mission at 90-m resolution (data access: http://hydrosheds.cr.usgs.gov) were used to exclude forested areas in the southern Amazon above 500-m elevation or on slopes >10%.

We selected four Laser 3 operation periods for the GLAS analysis. Two laser operation periods captured early dry season conditions (L3c, May to June 2005; L3f, May to June 2006), and two laser operation periods covered the late dry season across the southern Amazon (L3a, October 2004; L3i, October 2007). Data from L3a, L3c, L3f and L3i also had similar footprint characteristics (diameter, circularity and radial energy distribution). Differences in Laser 3 transmit energies between L3a and L3i do not impact the estimates of WCRH and apparent reflectance because these metrics are normalized by the transmit energy. The GLA09 and GLA14 standard data products (data access: http://nsidc.org) were used to assemble information on the location, laser energy, atmospheric backscatter, apparent reflectance and waveform characteristics for GLAS footprints over Amazon forests. GLAS data parameters were used to screen lidar footprints with cloud contamination, weak or saturated energies, or specular reflections from water. Specifically, we used the offset from the digital elevation model (< 70 m), pulse width (< 100 m), WCRH (< 1), apparent reflectance (> 0.45, < 1), and a threshold value in the integrated backscatter ($< 3.5 \times 10^{-6}$) to select cloud-free, high-quality ICESat data. In addition, we used MODIS aerosol optical thickness (AOT <0.09) data from the MOD09CMG product (E. Vermote, unpublished data) from the same date of GLAS observations to further screen the lidar data for high aerosol conditions. Finally, GLAS data from June and October laser periods were 'paired' using a 0.02° search radius to select

footprints from adjacent orbits. This paired subset of high-quality GLAS data ensured a similar spatial distribution of lidar footprints across the southern Amazon in early and late dry season conditions. The total number of GLAS footprints was 74,638, equally divided between June (L3c = 22,528, L3f = 14,791) and October (L3a = 20,786, L3i = 16,533).

MODIS analysis. We used Terra and Aqua MODIS data from 2003–08 to evaluate seasonal changes in canopy reflectance at ICESat footprint locations in eastern Amazonia. Daily red and NIR surface reflectances, sun-sensor geometry, and data quality flags were drawn from the Collection 5 MOD09GA and MYD09GA standard products at 1-km spatial resolution for two $10^\circ \times 10^\circ$ spatial tiles (H11V09 and H12V09, data access: https://lpdaac.usgs.gov). MODIS data were screened for high aerosols and cloud cover using the MOD09GA and MYD09GA data quality flags, and low-aerosol conditions (AOT <0.09) were confirmed using AOT estimates retrieved from the MOD09CMG product (E. Vermote, unpublished data). Fixed thresholds were also used to select MODIS observations with low red reflectance (< 0.2), NIR reflectance typical of vegetated surfaces ($0.1 < \mathrm{NIR} < 0.6$), and low view zenith angles ($<60^\circ$). Finally, an iterative outlier removal procedure was used to eliminate remaining observations with cloud or aerosol contamination. Outliers were identified as NDVI values > 2 standard deviations from the median NDVI value per pixel, per month. These outlier values were removed, and the process was repeated two more times to remove any residual cloud or aerosol-contaminated data. The resulting data set included 197,651 pixels across the southern Amazon. Larger data volumes could be achieved with alternative approaches for cloud and aerosol screening[46].

Each month, high-quality MODIS data from Terra and Aqua were combined to estimate the bidirectional reflectance distribution function (BRDF) and perform a per-pixel correction for variations in sun-sensor geometry. The BRDF correction uses Ross-Li-Maignan model, revised to account for the hot-spot effect[25,47]:

$$\rho(\theta_s,\theta_v,\phi) = k_0 + k_1 F_1(\theta_s,\theta_v,\phi) + k_2 F_2(\theta_s,\theta_v,\phi)$$

Surface reflectance (ρ) at a specified θ_s, θ_v, and ϕ is modelled as a function of volumetric (F_1) and geometric scattering (F_2). The volumetric scattering kernel (F_1) is based on the Rossthick function, corrected for the hot spot, and the geometric kernel (F_2) is based on the Li-sparse reciprocal function[25]. The model equation can be rewritten to highlight the contribution of the volumetric kernel (k_1/k_0) and geometric kernel (k_2/k_0) to the overall signal: :

$$= k_0 \left[1 + \frac{k_1}{k_0} F_1(0_s,0_v,\phi) + \frac{k_2}{k_0} F_2(0_s,0_v,\phi) \right]$$

The k_0, k_1 and k_2 parameters were inverted for red and NIR reflectances from all cloud free and low aerosol MODIS data on a per-pixel basis for all dry season months during 2003–08. A threshold of ≥ 20 observations per pixel, per month was set to ensure a robust statistical inversion. These BRDF parameters were then used to normalize both red and NIR reflectance values to a constant solar ($\theta_s = 30^\circ$) and view geometry ($\theta_v = 0^\circ$) for observations in all months. Normalization of sun-sensor geometry in this approach differs from previous efforts to correct MODIS data for BRDF[48]. Finally, NDVI and a two-band version of EVI[30] were calculated using the normalized red and NIR reflectance data.

Uncertainty estimation. We estimated the root mean square error (RMSE) of the MODIS surface reflectance product based on mean values of red (0.02) and NIR (0.33) reflectance over Amazon forests[49]. Measurement error was propagated to EVI and NDVI using a Monte Carlo sensitivity analysis approach. The RMSE of MODIS EVI (0.56) was 0.036, and the RMSE of MODIS NDVI (0.89) was 0.033. The root mean square model error was approximately one-third as large as measurement error. Assuming independence, total error is approximately 0.035 to 0.037 for both EVI and NDVI, or approximately 6% of mean EVI and 4% of NDVI. Seasonal differences in uncorrected MODIS EVI data exceed this error range (~0.1), while seasonal differences in corrected MODIS EVI data do not (see Fig. 3).

31. Palace, M., Keller, M., Asner, G. P., Hagen, S. & Braswell, B. Amazon forest structure from IKONOS satellite data and the automated characterization of forest canopy properties. *Biotropica* **40,** 141–150 (2008).
32. Asner, G. P. *et al.* Estimating canopy structure in an Amazon forest from Laser Range Finder and IKONOS satellite observations. *Biotropica* **34,** 483–492 (2002).
33. Hunter, M. O., Keller, M., Vitoria, D. & Morton, D. C. Tree height and tropical forest biomass estimation. *Biogeosciences Discuss.* **10,** 10491–10529 (2013).
34. King, D. A. Allometry of saplings and understory trees of a Panamanian forest. *Funct. Ecol.* **4,** 27–32 (1990).
35. Osunkoya, O. O. *et al.* Comparative height crown allometry and mechanical design in 22 tree species of Kuala Belalong rainforest, Brunei, Borneo. *Am. J. Bot.* **94,** 1951–1962 (2007).
36. Keller, M., Palace, M. & Hurtt, G. C. Biomass estimation in the Tapajos National Forest, Brazil: examination of sampling and allometric uncertainties. *For. Ecol. Manage.* **154,** 371–382 (2001).
37. Feldpausch, T. R. *et al.* Height-diameter allometry of tropical forest trees. *Biogeosciences* **8,** 1081–1106 (2011).
38. Saatchi, S. S. *et al.* Benchmark map of forest carbon stocks in tropical regions across three continents. *Proc. Natl Acad. Sci. USA* **108,** 9899–9904 (2011).
39. Baccini, A. *et al.* Estimated carbon dioxide emissions from tropical deforestation improved by carbon-density maps. *Nature Clim. Change* **2,** 182–185 (2012).
40. North, P. R. J. Three-dimensional forest light interaction model using a Monte Carlo method. *IEEE Trans. Geosci. Rem. Sens.* **34,** 946–956 (1996).
41. Huete, A. R., Ferreira, L. & Miura, T. LBA-ECO LC-19 Field Measurements 2002: Biophysical & Soil Parameters. http://www.lbaeco.org (2008).
42. Hofton, M. A., Minster, J. B. & Blair, J. B. Decomposition of laser altimeter waveforms. *IEEE Trans. Geosci. Rem. Sens.* **38,** 1989–1996 (2000).
43. Harding, D. J. & Carabajal, C. C. ICESat waveform measurements of within-footprint topographic relief and vegetation vertical structure. *Geophys. Res. Lett.* **32,** L21S10 (2005).
44. Morton, D. C. *et al.* Mapping canopy damage from understory fires in Amazon forests using annual time series of Landsat and MODIS data. *Remote Sens. Environ.* **115,** 1706–1720 (2011).
45. Morton, D. C., Le Page, Y., DeFries, R., Collatz, G. J. & Hurtt, G. C. Understorey fire frequency and the fate of burned forests in southern Amazonia. *Phil. Trans. R. Soc. Lond. B* **368** (2013).
46. Hilker, T. *et al.* Remote sensing of tropical ecosystems: atmospheric correction and cloud masking matter. *Remote Sens. Environ.* **127,** 370–384 (2012).
47. Vermote, E. F., Justice, C. & Breon, F.-M. Towards a generalized approach for correction of the BRDF effect in MODIS directional reflectance. *IEEE Trans. Geosci. Rem. Sens.* **47,** 898–908 (2009).
48. Schaaf, C. B. *et al.* First operational BRDF, albedo nadir reflectance products from MODIS. *Remote Sens. Environ.* **83,** 135–148 (2002).
49. Vermote, E. F. & Kotchenova, S. Atmospheric correction for the monitoring of land surfaces. *J. Geophys. Res. D Atmospheres* **113,** D23S90 (2008).

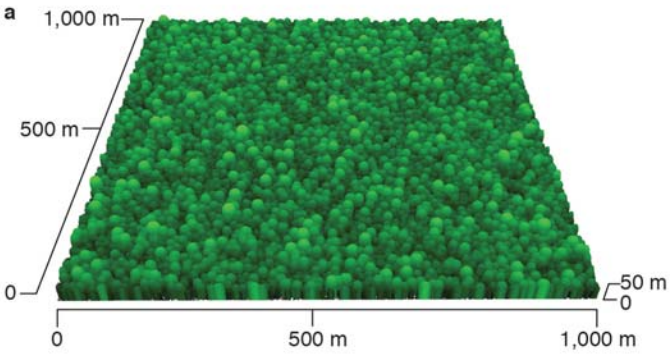

b

	MODIS		MODIS		ICESat	
	ρ_{Red}	τ_{Red}	ρ_{NIR}	τ_{NIR}	ρ_{NIR}	τ_{NIR}
Leaves	0.039	0.019	0.361	0.371	0.368	0.389
Litter						
KM67	0.052	-	0.225	-	0.343	-
KM83-1	0.144	-	0.302	-	0.424	-
KM83-2	0.172	-	0.395	-	0.538	-

c

Model Parameters	Lidar Simulations	June Conditions
LAI	4.5, 5.5, 6.5	4.5
ρ_{NIR} Leaf	0.29, 0.39, 0.49	0.39
τ_{NIR} Leaf	0.37	0.37
ρ_{NIR} Litter	0.34, 0.44, 0.54	0.34
ρ_{NIR} Bark	0.39	0.39

d

Model Parameters	Optical Simulations	June Conditions
LAI	4.5, 5.5, 6.5	4.5
ρ_{NIR} Leaf	0.39, 0.49	0.39
τ_{NIR} Leaf	0.37, 0.47	0.37
ρ_{Red} Leaf	0.05	0.05
τ_{Red} Leaf	0.015	0.015
ρ_{NIR} Litter	0.05, 0.30, 0.55	0.30
ρ_{Red} Litter	0.13	0.13
ρ_{NIR} Bark	0.39	0.39
Solar Zenith Angle	20°, 30°, 40°	40°
View Zenith Angle	0° - 60°	15°
Relative Azimuth	0° - 180°	0°

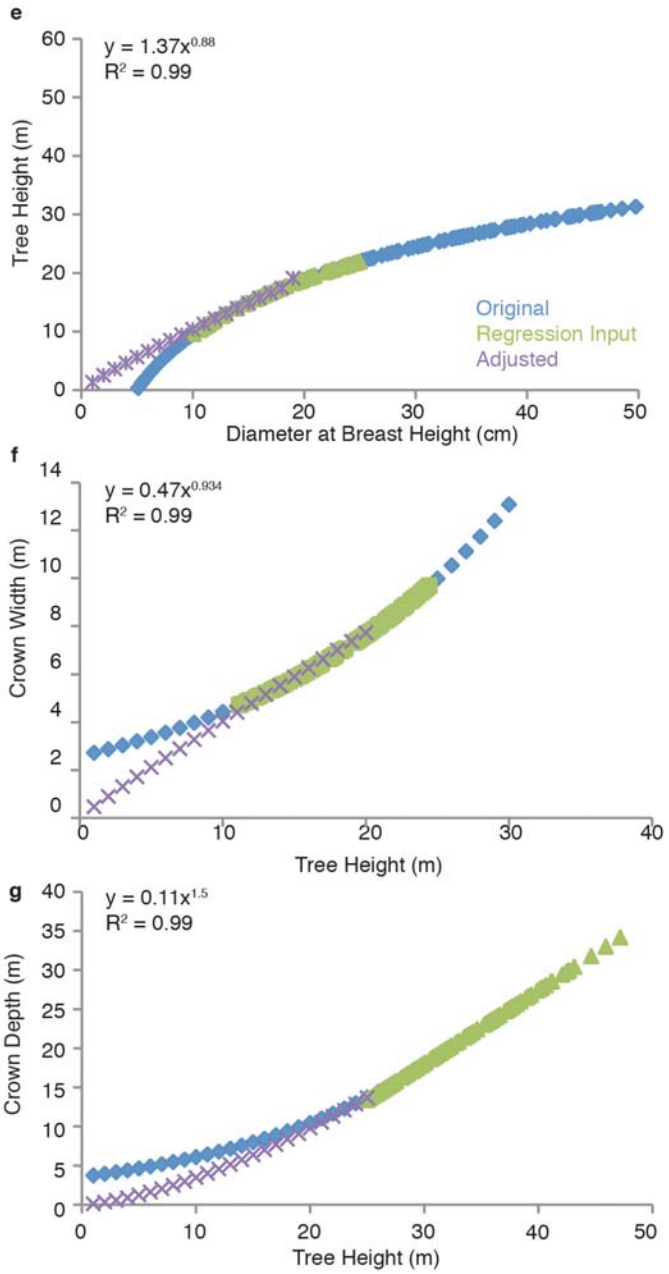

Extended Data Figure 1 | Synthetic Amazon forest developed from field measurements of forest structure and reflectance properties. **a**, Oblique view of the 1 km × 1 km synthetic forest. **b**, Reflectance (ρ) and transmittance (τ) properties of Amazon leaves (G. P. Asner, unpublished data) and litter[41] at MODIS (red, 620–670 nm; NIR, 841–876 nm) and ICESat (NIR, 1064 nm) wavelengths. **c**, **d**, Parameter values for lidar and optical radiative transfer simulations. Field measurements of ρLitter differ slightly at optical (860 nm) and lidar (1064 nm) NIR wavelengths (see **b**). June conditions were used to estimate early dry season (baseline) lidar and optical remote sensing metrics with FLIGHT. **e**–**g**, Height-diameter relationships (**e**) and crown depth (**f**) and width (**g**) estimates for small trees (< 20-cm diameter at breast height) were derived from allometric relationships for larger trees (>20-cm diameter at breast height) using regression with a power-law function.

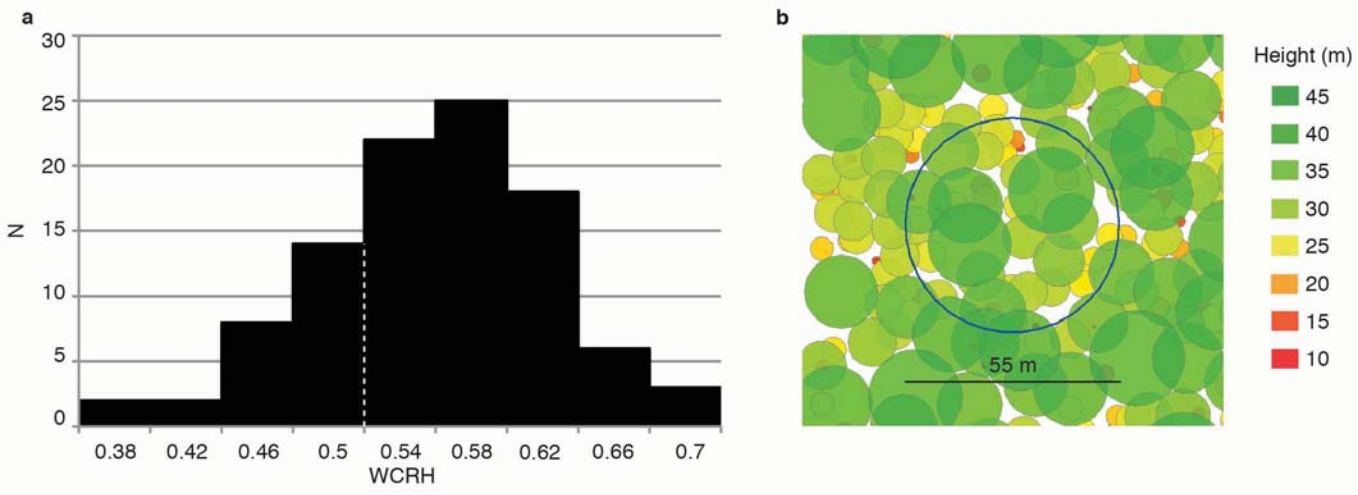

Extended Data Figure 2 | FLIGHT model simulations of GLAS lidar waveforms. **a**, Distribution of modelled waveform centroid relative height (WCRH) for 100 simulated GLAS lidar footprints located at the centre of each 100 × 100 m grid box of the synthetic Amazon forest. **b**, Nadir view of the waveform selected for FLIGHT model simulations (blue outline). The dashed vertical line in **a** indicates the June WCRH (0.519) for the footprint location in **b**.

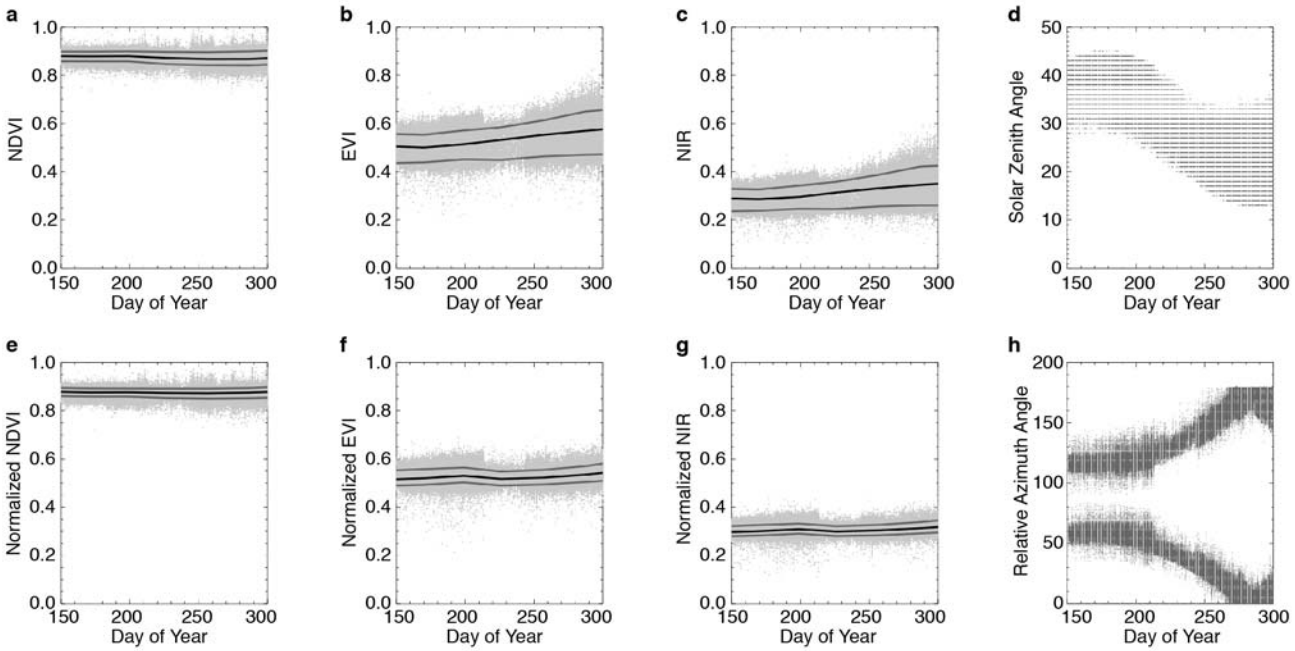

Extended Data Figure 3 | Seasonal variability in MODIS surface reflectance, vegetation indices, and sun-sensor geometry. Seasonal distributions of NDVI, EVI and near-infrared (NIR) reflectance for uncorrected (**a**–**c**) and corrected (**e**–**g**) MODIS 1 km data from 2003–08, in which corrected MODIS data have been normalized to a consistent sun-sensor geometry. Lines denote the median (black) and upper and lower quartile median values (grey) for uncorrected and corrected MODIS observations. The decrease in solar zenith angle between day of year 150 and 300 (**d**) increases the frequency of observations near the principal plane (**h**, $\phi = 0^{\circ}$, $\phi = 180^{\circ}$).

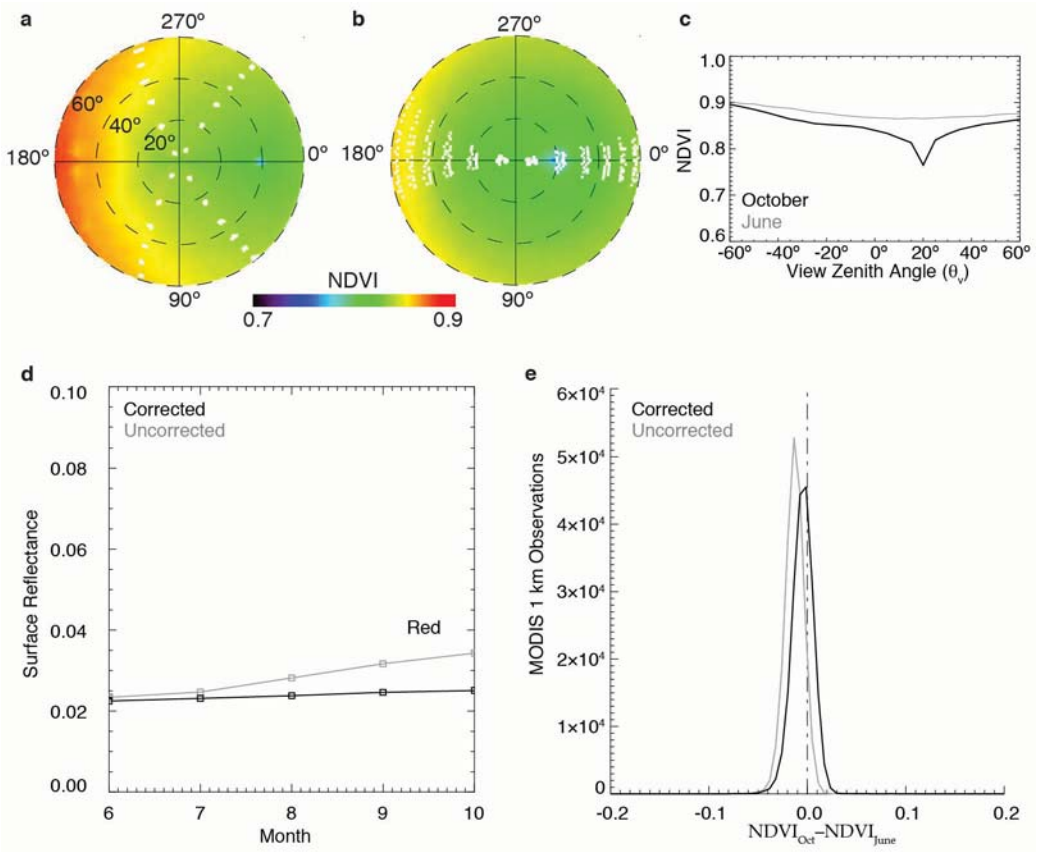

Extended Data Figure 4 | Impact of changing MODIS sun-sensor geometry on NDVI. **a**–**c**, Seasonal changes in sun-sensor geometry decrease MODIS NDVI over Amazon forest between June and October. As for EVI (see Fig. 1), modelled directional anisotropy of the MODIS NDVI over southern Amazon forests is stronger in June (**a**) than October (**b**), but the realized bidirectional reflectance effect in MODIS observations is greater in October (**b**, **c**) when the Terra and Aqua MODIS instruments sample in the principal plane ($\phi = 0^{\circ}$, $\phi = 180^{\circ}$). For NDVI, the hot spot effect near $\theta_v = 20^{\circ}$ increases red reflectance, thereby lowering NDVI values at these viewing angles. **d**, Seasonal profile of red reflectance for uncorrected (grey) and corrected (black) MODIS 1 km data in southern Amazonia. Values indicate the upper quartile median monthly red reflectance from all Terra and Aqua MODIS observations in 2003–08 ($n = 197{,}651$). **e**, Per-pixel changes in uncorrected (grey) and corrected (black) MODIS NDVI between October and June for all forested areas in southern Amazonia. Small seasonal decreases in MODIS NDVI data were eliminated after normalizing the sun-sensor geometry during the June to October dry season.

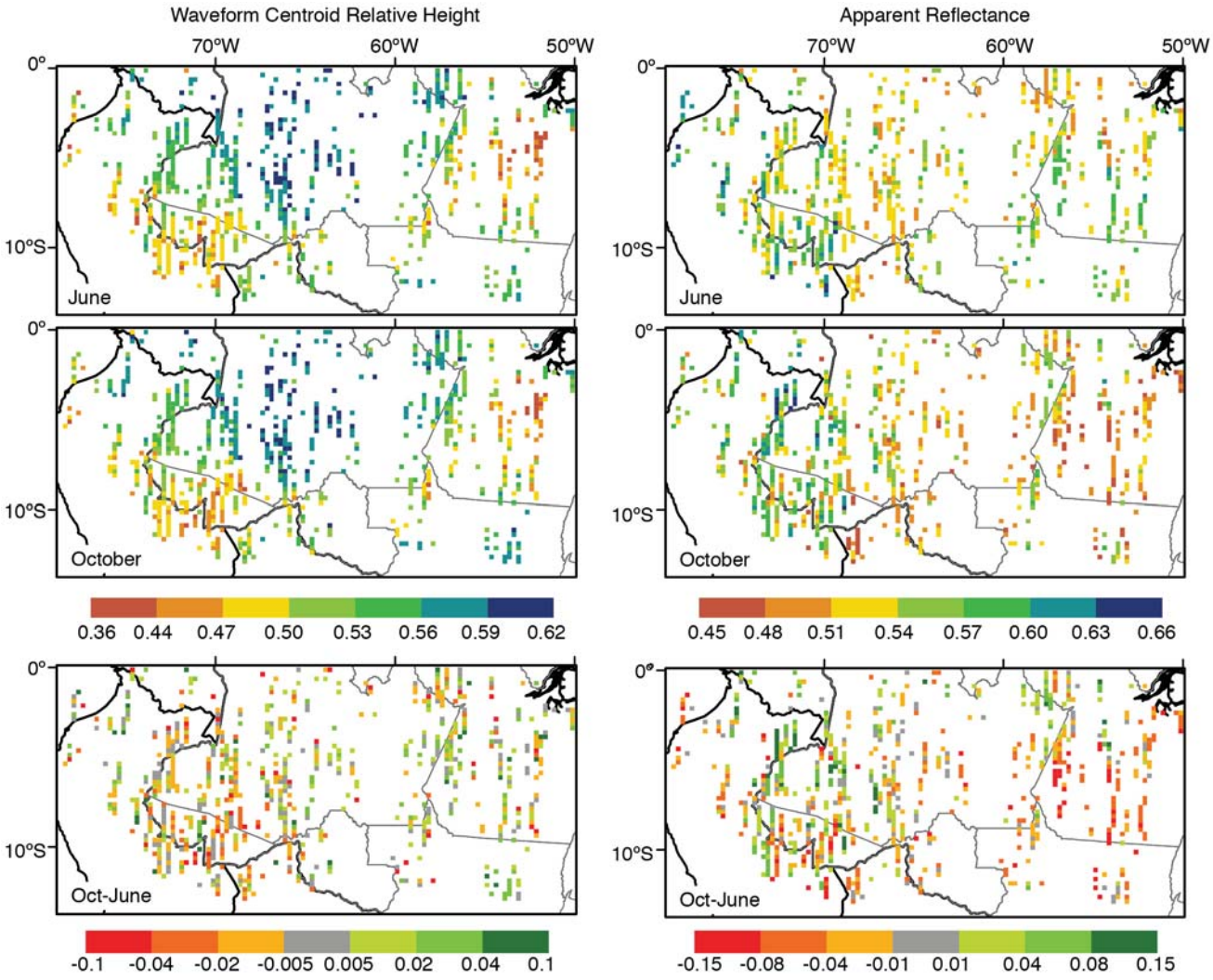

Extended Data Figure 5 | Spatial pattern of seasonal changes in GLAS lidar metrics. **a**–**f**, June, October, and difference maps (October minus June) of WCRH (**a**–**c**) and 1064 nm apparent reflectance (**d**–**f**) for 0.25° grid cells in southern Amazonia with ≥ 10 pairs of June and October GLAS footprints. White cells indicate non-forest areas or grid cells with <10 GLAS lidar footprints in one or both months.

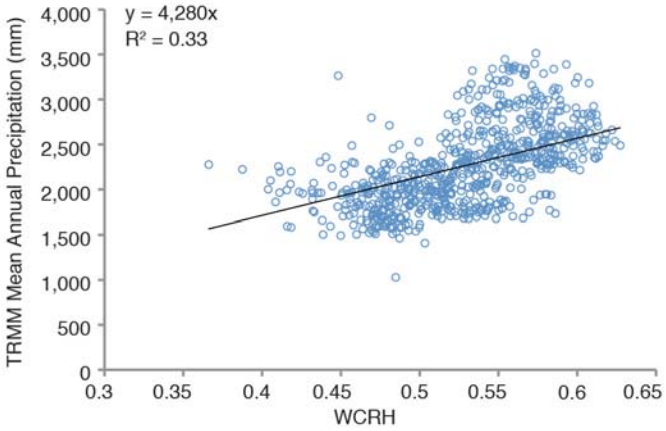

Extended Data Figure 6 | Correlation between GLAS lidar WCRH and mean annual precipitation. Values indicate mean June WCRH and mean annual precipitation (September to August, 1997–2009) from the tropical rainfall measurement mission (TRMM) 3B43v6 product for 0.25° cells with ≥ 10 GLAS footprint pairs ($n = 728$, see Extended Data Fig. 5).

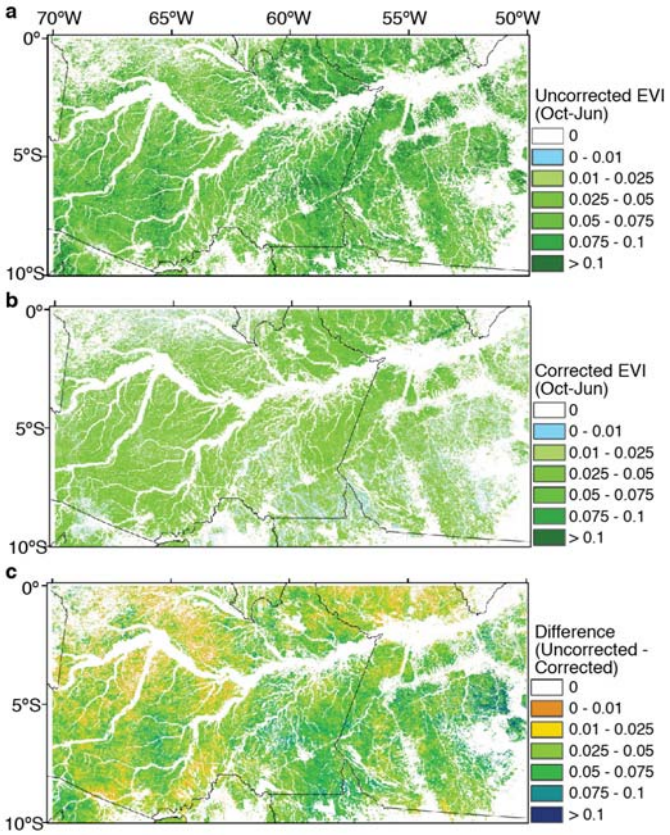

Extended Data Figure 7 | Maps of seasonal amplitude in uncorrected and corrected MODIS EVI data. **a**, Seasonal amplitude in uncorrected MODIS EVI data (October minus June) for two $10^{\circ} \times 10^{\circ}$ spatial tiles in southern Amazonia (H11V09, H11V10). **b**, Seasonal amplitude in corrected EVI data (October minus June), using a single BRDF inversion model to normalize changes in sun-sensor geometry for all Amazon forest pixels per tile, per month. Instead of modelling BRDF on a per-pixel basis (see Fig. 3, Extended Data Figs 3, 4 and 8), this map reflects the reduction in the seasonal amplitude of EVI using generic BRDF models derived from all cloud-free MODIS data per tile, per month. **c**, The difference in the seasonal amplitude of MODIS EVI (uncorrected minus corrected) is positive, highlighting how changes in sun-sensor geometry generate the apparent green up phenomenon. White regions indicate non-forest cover types.

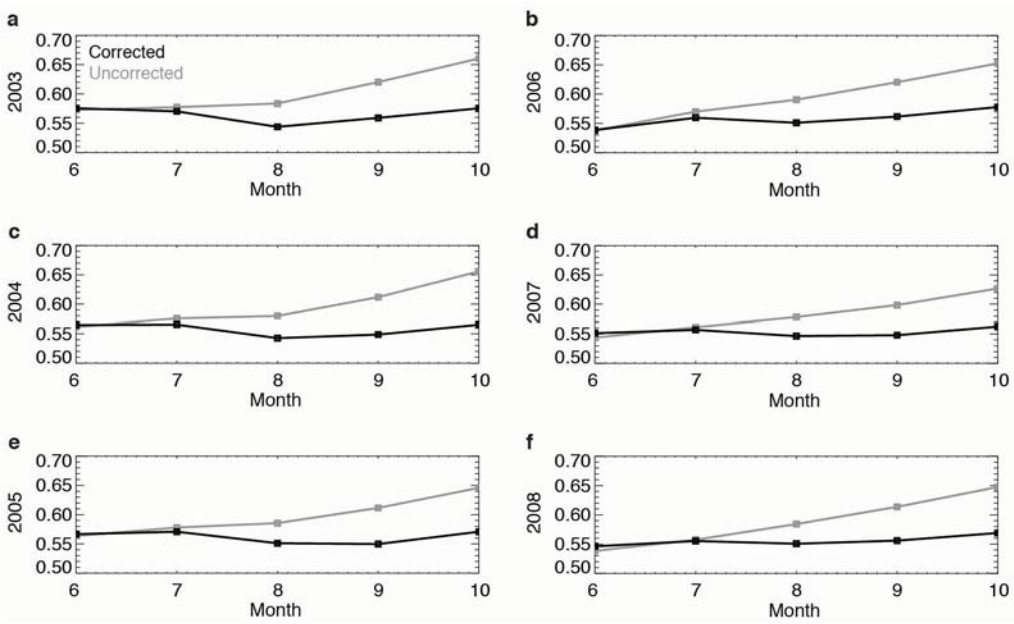

Extended Data Figure 8 | Interannual variability in MODIS EVI for southern Amazon forests in 2003–08. Values indicate the upper quartile median monthly EVI for uncorrected (grey) and corrected (black) MODIS data. Normalization of sun-sensor geometry reduced both seasonal and interannual variability in MODIS EVI over southern Amazon forests.

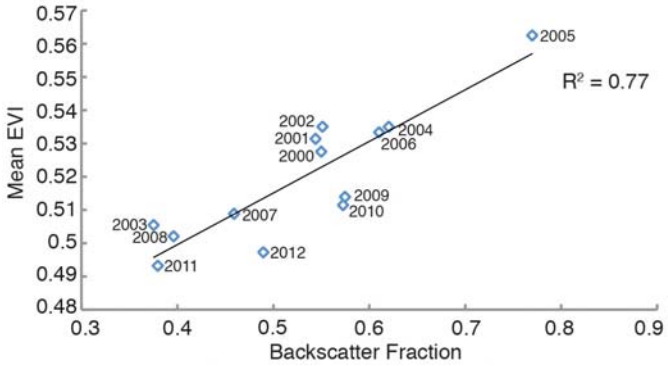

Extended Data Figure 9 | Contribution of variability in MODIS view geometry to interannual differences in EVI over Amazon forests. EVI and view zenith angle (θ_v) data from the MOD13A1 16-day composite product (data access: https://lpdaac.usgs.gov) are shown for spatial tile H11V09 when the Terra MODIS sensor was observing in the principal plane (October, day of year 273–288). The fraction of observations in the backscatter direction ($\theta_v > 0^\circ$) and mean EVI over forests were strongly correlated, highlighting the importance of sun-sensor geometry for interannual variability in uncorrected MODIS EVI data. The drought year of 2005 had the highest fraction of MODIS observations in the backscatter direction of any year during 2000–12.

Extended Data Table 1 | Sensitivity of lidar WCRH and optical vegetation indices (EVI, NDVI) to modelled seasonal changes in forest structure and reflectance properties

Model Parameter	Value	WCRH	EVI	NDVI
LAI	4.5	0.52	0.43	0.81
	5.5	0.55	0.43	0.82
	6.5	0.58	0.43	0.83
Litter (1064 nm)*	0.34	0.52		
	0.44	0.50		
	0.54	0.48		
Litter (860 nm)	0.05		0.38	0.79
	0.30		0.43	0.81
	0.55		0.48	0.83
Leaf†	0.29	0.50		
	0.39	0.52	0.43	0.81
	0.49	0.52	0.54	0.85

Optical data simulations reflect October illumination conditions ($\theta_s = 20^\circ$, $\theta_v = 15^\circ$, $\phi = 0^\circ$).
* Field measurements of ρLitter differ slightly between lidar (1064 nm) and optical (841–876 nm) NIR ranges (see Extended Data Fig. 1).
† FLIGHT model analyses in the optical domain did not include simulations with ρLeaf = 0.29.